Environmental Technology & Innovation 30 (2023) 103032

Contents lists available at ScienceDirect

Environmental Technology & Innovation

journal homepage: www.elsevier.com/locate/eti

Performance analysis of externally reflected photoreactor for CO_2 conversion to methanol using f-C_3N_4/ZnV_2O_6 S-scheme photocatalyst

Abdullah Bafaqeer [a,b], Muhammad Tahir [c,*], Nor Aishah Saidina Amin [a,*], Nader Al-Bastaki [d], Wahid Ali Hamood Altowayti [e], Hammam Abdurabu Thabit [f]

[a] Faculty of Chemical and Energy Engineering, Universiti Teknologi Malaysia, UTM, 81310, Johor Bahru, Malaysia
[b] Faculty of Chemical Engineering, Hadhramout University, Al-Mukalla, Hadhramout, Yemen
[c] Chemical and Petroleum Engineering Department, UAE University, P.O. Box 15551, Al Ain, United Arab Emirates
[d] Academic Affairs and Scientific Research, Kingdom University, P.O. Box 40434, Riffa, Kingdom of Bahrain
[e] Department of Biosciences, Faculty of Science, Universiti Teknologi Malaysia, UTM, 81310, Johor Bahru, Malaysia
[f] Department of Physics, Faculty of Science, Universiti Teknologi Malaysia, UTM, 81310, Johor Bahru, Malaysia

ARTICLE INFO

Article history:
Received 19 October 2022
Received in revised form 12 January 2023
Accepted 17 January 2023
Available online 20 January 2023

Keywords:
Photocatalytic activity
CO_2 reduction
CH_3OH
ZnV_2O_6/f-C_3N_4 S-scheme photocatalyst
Externally reflected photoreactor
Performance analysis

ABSTRACT

In this study, a novel externally reflected photoreactor was compared with a solar photoreactor for photocatalytic CO_2 conversion in liquid phase using proton-rich functionalized carbon nitride (f-C_3N_4) modified ZnV_2O_6 nanosheets. Effects of operating parameters such as reaction medium and catalyst loading were investigated to maximize yield rates. The performance of photoreactor for CO_2 photoconversion was higher in the presence of NaOH solution as a reducing agent than H_2O and $KHCO_3$ solution. ZnV_2O_6 modified with f-C_3N_4 (1:1) ratio registered the highest CH_3OH yield. In an externally reflected photoreactor, the maximum yield rate of CH_3OH over ZnV_2O_6/f-C_3N_4 (1:1) nanosheets was 4665.6 μmole g-cat^{-1}; 1.25 folds higher than solar photoreactor (3742.1 μmole g-cat^{-1}). The externally reflected photoreactor was found very efficient for photocatalytic CO_2 conversion due to its higher light harvesting efficiency compared to the solar photoreactor. The increased yield rates in externally reflected photoreactor were because the reflector provides greater photon flux for dynamic CO_2 reduction. Possible reaction mechanisms for photoconversion of CO_2 over ZnV_2O_6/f-C_3N_4 S-scheme photocatalyst were proposed in order to understand the function of the reflector and the movement of electrons and holes.

1. Introduction

The significant rise in the levels of atmospheric carbon dioxide (CO_2), considered as one of the greatest contributors to the greenhouse effect, has attracted substantial attention within the past few decades (Szamosvölgyi et al., 2022; Tahir and Tahir, 2022; Zhao et al., 2022). Several strategies have been utilized to reduce the impacts of CO_2, including reducing CO_2 emissions at the source (Aslam et al., 2021), capturing and storing CO_2 (Zahedi et al., 2022), and reusing CO_2 by converting it into useful chemicals and fuels (Sharma et al., 2022; Zhao et al., 2021). However, these technologies have drawbacks,

* Corresponding authors.
E-mail addresses: muhammad.tahir@uaeu.ac.ae (M. Tahir), noraishah@cheme.utm.my (N.A.S. Amin).

https://doi.org/10.1016/j.eti.2023.103032

such as the need for high electrical power and high temperatures to split the stable CO_2 molecule, unsustainability, raw material constraints, and high operating costs (Jebaseelan et al., 2021; Kumar et al., 2021).

Recent interest has been focused on photocatalysis using light irradiation because it occurs at low temperatures and normal pressure (Nguyen et al., 2022; Thabit et al., 2022; Wang et al., 2022b). The CO_2 reduction by photo-technology would meet the existing energy needs and address environmental issues (Idris et al., 2022; Yuan et al., 2021; Zhang et al., 2022a). However, the performance of photocatalytic activity and selectivity is lower for CO_2 reduction that is needed to be improved. The efficiency of photocatalytic process can be enhanced by develop highly effective semiconductor materials (Kumar et al., 2023; Lee et al., 2023) and design of photoreactors (Khan and Tahir, 2019; Liang et al., 2020; Ng et al., 2021; Tahir and Amin, 2017).

Among the newly emerged semiconductor materials, 2D layered graphitic carbon nitride (g-C_3N_4) has been widely examined for photocatalytic conversion of CO_2 because of its higher light absorption, and good reduction potential for CO_2 conversion to several products (Arumugam et al., 2022; Bafaqeer et al., 2021). However, CO_2 conversion rate of g-C_3N_4 is lower due to high recombination rate of charge carrier (Li et al., 2022b). The efficiency of 2D g-C_3N_4 can be enhanced by several methods which include doping with metal and nonmetal elements (Hussain et al., 2022), surface modification (Tahir and Tahir, 2020) and coupling with other semiconductors (Cao et al., 2023; Wang et al., 2023). Furthermore, the construction of an S-scheme photocatalytic system has drawn a lot of attention because of its ideal effectiveness in enhancing the photocatalytic efficiency (Wang et al., 2022c; Xu et al., 2022; Zhang et al., 2022b). From this perspective, the construction of S-scheme semiconductors like ZnO/g-C_3N_4 (Sayed et al., 2022), Bi_3NbO_7/g-C_3N_4 (Wang et al., 2022a), g-C_3N_4/BiOI (Li et al., 2022b), $ZnIn_2S_4$/g-C_3N_4 (Li et al., 2022a) and $CuWO_4$/g-C_3N_4 (Lu and Wang, 2023) have exhibited significantly promoted photocatalytic activity toward conversion of CO_2 to fuels. We recently reported ZnV_2O_6 nanosheets as a promising photocatalyst for photocatalytic CO_2 to CH_3OH conversion under visible light (Bafaqeer et al., 2018b). This was because of a unique 2D ZnV_2O_6 interfacial structure that increases the transfer rate of photogenerated holes and electrons, as well as an appropriate band structure and strong visible absorption, resulting in increased photocatalytic activity. Combining 2D ZnV_2O_6 nanosheets with functionalized g-C_3N_4 nanocomposite would develop S-scheme heterojunction, which may not only improve charge separation performance but also provides good redox potential for selective CO_2 conversion under visible light. Thus, it is highly desirable to create functionalized g-C_3N_4 modified ZnV_2O_6 S-scheme photocatalyst to improve the photocatalytic conversion of CO_2 into fuels under visible-light.

The design of photoreactors is gradually improving, whereas slurry, membrane, and fixed-bed photoreactors are used for photocatalytic processes. The most popular reactors are slurry reactors and include three phase system where the catalyst bed is in a fluidized form and agitated to increase mass transfer between catalyst and reactants, therefore providing large surface area to be illuminated (Ješić et al., 2021). Photocatalysts in fixed bed photo-reactors are positioned inside the photoreactor near the light or directly on the photoreactor wall, immobilized on the supporting materials such as plate, fibers, beads, monolith, optical fibers etc. (Foulady-Dehaghi and Behpour, 2020; Yazdani et al., 2018). Although fixed bed photoreactors have a high gas production and do not need the catalyst to be separated, light dispersion has been a challenge. Two chambers or towers in the membrane photoreactors are separated from one another by a membrane (Baniamer et al., 2021; Khan and Tahir, 2019). The limited charge and mass transfer has been a cause of worry even though the reaction in membrane photoreactors is extremely tightly controlled and does not allow for backward reaction. Therefore, it is highly desirable to develop photoreactors with high efficiency to enhance photocatalytic reduction of CO_2 to fuels.

In this work, a novel externally reflected photoreactor was developed for photocatalytic CO_2 reduction into fuels. The performance of an externally reflected photoreactor and solar photoreactor was compared over proton-rich C_3N_4 modified ZnV_2O_6 S-scheme photocatalyst. The stability test of ZnV_2O_6/f-C_3N_4 S-scheme photocatalyst in an externally reflected photoreactor and possible reaction mechanism of CO_2 conversion was also deliberated.

2. Experimental

2.1. Synthesis of f-C_3N_4

Typically, 5 g of melamine was placed in a crucible and heated in a muffle furnace at 550 °C for duration of 2 h under an air atmosphere. The yellow powder obtained was grounded into fine powder and named g-C_3N_4. After that, g-C_3N_4 and nitric acid are mixed and stirred for preferably 2 h. The existence of numerous –C–N–motifs in the g-C_3N_4 allows it to be easily functionalized by nitric acid. The precipitates from the mixture are then dried at a temperature of 80 °C for approximately 12 h to produce a functionalized graphitic carbon nitride (f-C_3N_4).

2.2. Synthesis of ZnV_2O_6/f-C_3N_4 nanosheets

As previously described, a one-pot solvothermal technique was used to prepare the ZnV_2O_6 photocatalyst (Bafaqeer et al., 2018b). The ZnV_2O_6/f-C_3N_4 nanosheets were fabricated by a one-step solvothermal process. Typically, 2.052 mmol of ammonium metavanadate is added into 20 ml of DMF. Next, the 1.09 mmol zinc acetate is added after 10 mins of stirring which is then followed by the addition of oxalic acid, wherein the ratio of oxalic acid to NH_4VO_3 is suitably 1:3. At the same time, the f-C_3N_4 is mixed with DMF and stirred for approximately 10 mins. After that, f-C_3N_4 mixture was

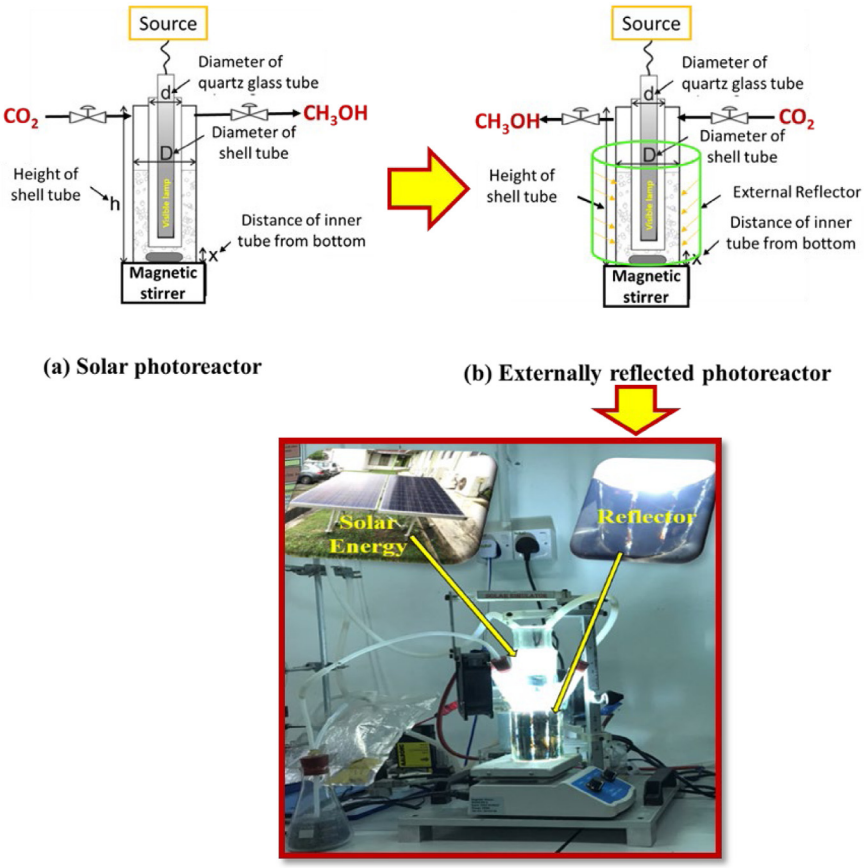

Fig. 1. Schematic of experimental setup for photocatalytic CO_2 conversion with H_2O: (a) Solar photoreactor and (b) Externally reflected photoreactor.

added to the above solution and stirred for approximately 30 mins. The mixed solution was then reacted in an autoclave at a suitable temperature range of 180 to 200 °C for approximately 24 h. The precipitates are washed with absolute ethanol and distilled water. The resulting precipitates are then dried at a preferred temperature of 100 °C for approximately 12 h to produce the ZnV_2O_6/f-C_3N_4 nanosheets.

2.3. Materials characterization

The XRD (Rigaku, Cu Kβ radiation) was used to measure the crystalline structures of the produced photocatalysts. The structure and morphology were observed by a field emission scanning electron microscopy (FE-SEM, Zeiss Crossbeam 340 system) and a high-resolution transmission electron microscope (HRTEM, HITACHI-HT7700 system). The Ultraviolet–visible (UV–vis) diffuse reflectance absorbance spectra of the photocatalysts were carried out on an Agilent, Cary 100 UV–vis spectrophotometer integrated with a sphere. Photoluminescence (PL) spectra of photocatalysts were recorded at room temperature utilizing a laser of 325 nm as the excitation source.

2.4. Photocatalytic performance evaluation

The effectiveness of a solar photoreactor's photocatalytic performance for converting CO_2 in liquid phase was compared to that of an externally reflected photoreactor. Fig. 1(a) shows a schematic representation of the solar photoreactor. The apparatus utilized as the photoreactor for the visible light photoreaction included a Pyrex glass reactor clamped to a retort stand, a cold trap, and a heating stirrer. The Pyrex glass reactor features three angled joints, a 150 ml volume, and an effective length of 200 mm. Each of the three Pyrex glass reactor's angled joints served as a gas intake, gas exit, and sample port. A Teflon tube was connected to the flow metre, which was supplying the Pyrex glass reactor with CO_2 from the gas tank. The Teflon tube supplying the CO_2 into the Pyrex glass reactor was passed through a plastic cork, which was fitted into the angled joint of the Pyrex glass reactor in order to prevent the gas from escaping. Regarding the sampling port, a Teflon tube was linked to the Pyrex glass and the sampling port tap through the plastic cork. In order to allow produced gases to escape during the photoreaction process, a Teflon tube was linked to the gas outlet tap and the Pyrex glass

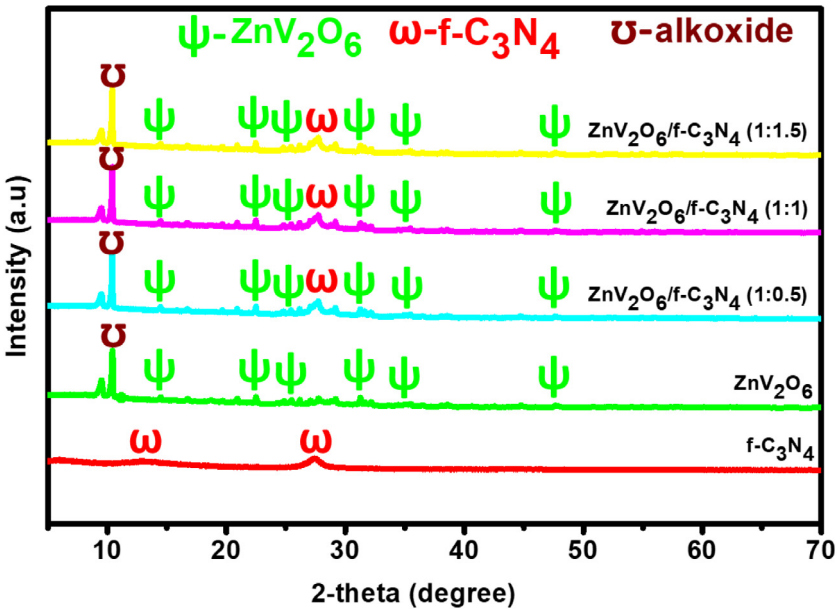

Fig. 2. XRD pattern of f-C_3N_4, ZnV_2O_6, ZnV_2O_6/f-C_3N_4 (1:0.5), ZnV_2O_6/f-C_3N_4 (1:1) and ZnV_2O_6/f-C_3N_4 (1:1.5) samples.

through the plastic cork. The cold trap was a double-jacketed Pyrex glass container with two angled joints for the entry and exit of cooling water. To cool the heat produced by the lamp and filter infrared heat, the HID Xe lamp was positioned inside the cold trap's hollow. The two angled connections at the top of the cold trap were employed by a circulation chiller to circulate chilling water to the cold trap. The cooling water entered at the cooling water intake and exited at the water outlet. The mixture of the reaction medium and the catalyst powder placed in the reactor vessel was stirred using a heated stirrer and a magnetic bar. The schematic of the externally reflected photoreactor is exhibited in Fig. 1(b). The design of externally reflected photoreactor is the extension of currently available solar photoreactor. However, the available solar photoreactor operates under visible light irradiations with low efficiency. So, the solar photoreactor was modified with an external reflector for improved efficiency. The reflector was made from parabolic mirror to reflect the light to provide higher light irradiations to get higher reduction of CO_2 and increase yield rates.

3. Results and discussion

3.1. Photocatalysts characterization

The XRD patterns of the bare and calcined ZnV_2O_6 have previously been described (Bafaqeer et al., 2018a). The ZnV_2O_6 displayed several diffraction peaks, which are characteristics of ZnV_2O_6 as shown in Fig. 2. Also, the XRD pattern of the ZnV_2O_6 exhibits pronounced peak located at 2θ of 10.0° belonging to metal alkoxide, because of as prepared catalysts without calcination at higher temperature (Yin et al., 2017; Zhang et al., 2017). The f-C_3N_4 exhibited two distinct peaks at 2θ of 27.53° and 12.96°. The (002) plane was allocated the strong distinct peak at 2θ of 27.53°. In contrast, the weak distinct peak at 2θ of 12.96° can be assigned to the (100) plane. The existence of these two distinct peaks of f-C_3N_4 validates its identity. For the ZnV_2O_6/f-C_3N_4 nanocomposite, the XRD patterns show a combination of the two sets of diffraction data for both ZnV_2O_6 and f-C_3N_4. Thus, the results indicated the presence of two phases, ZnV_2O_6 and f-C_3N_4, in the nanocomposite sample. The peaks of the ZnV_2O_6/f-C_3N_4 nanocomposite were unaffected by the increase in f-C_3N_4 content.

The morphology of ZnV_2O_6, f-C_3N_4 and ZnV_2O_6/f-C_3N_4 nanocomposite samples was investigated utilizing field emission scanning electron micrographs (FESEM) as shown in Fig. 3. It can be seen in Fig. 3(a) that the FESEM image of ZnV_2O_6 contains large number of sheets with 2D nanostructures. As depicted in Fig. 3(b), after protonation with nitric acid, clear exfoliated sheets of g-C_3N_4 with hollows and lamellar structures were formed. Fig. 3(c) shows the f-C_3N_4 sheets are uniformly dispersed over ZnV_2O_6 nanosheets. This demonstrates the effective interaction of f-C_3N_4 and ZnV_2O_6 nanosheets in forming the heterojunction. The EDX spectra in Fig. 3(d) further confirm the existence of all of the elements in the ZnV_2O_6/f-C_3N_4 nanocomposite. The existence of Pt was because of platinum utilized for FESEM analysis. The morphology of ZnV_2O_6/f-C_3N_4 nanosheets was further elucidated utilizing HRTEM, and the results are illustrated in Fig. 3(e) and (f). As depicted in Fig. 3(e), the HRTEM image clarifies that the f-C_3N_4 is effectively deposited on the surface of ZnV_2O_6 nanosheets. Exfoliated ZnV_2O_6 nanosheets with consistent f-C_3N_4 distribution were also shown to generate the

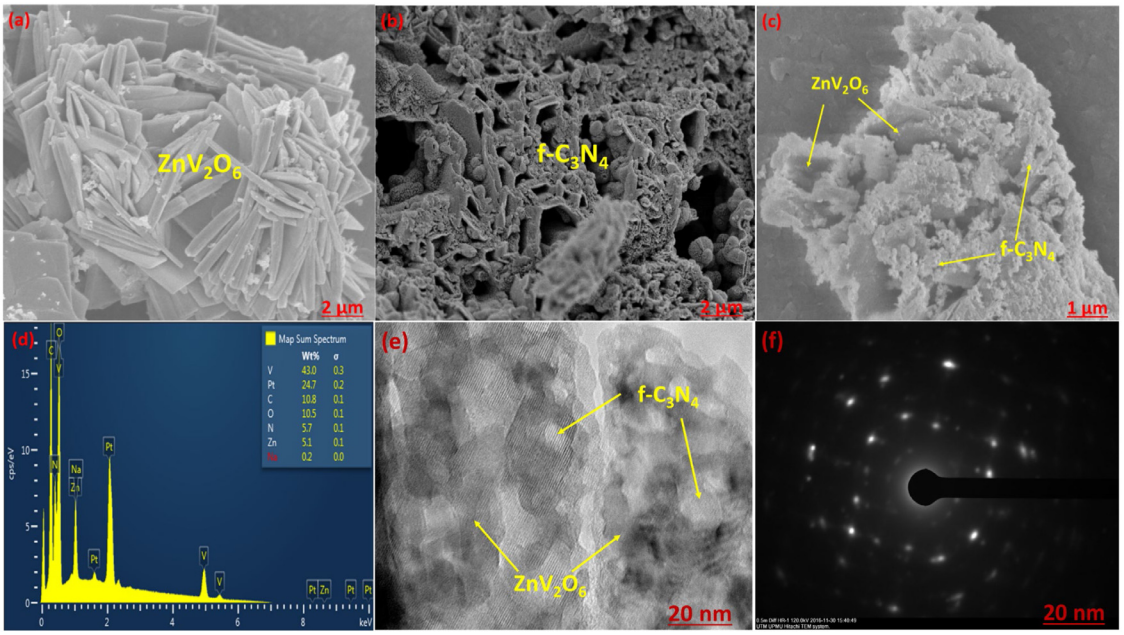

Fig. 3. FE-SEM images of (a) ZnV_2O_6; (b) f-C_3N_4; (c) ZnV_2O_6/f-C_3N_4; (d) EDX plots with elements composition; HRTEM images of (e) ZnV_2O_6/f-C_3N_4; (f) SAED pattern of the ZnV_2O_6/f-C_3N_4 nanocomposite.

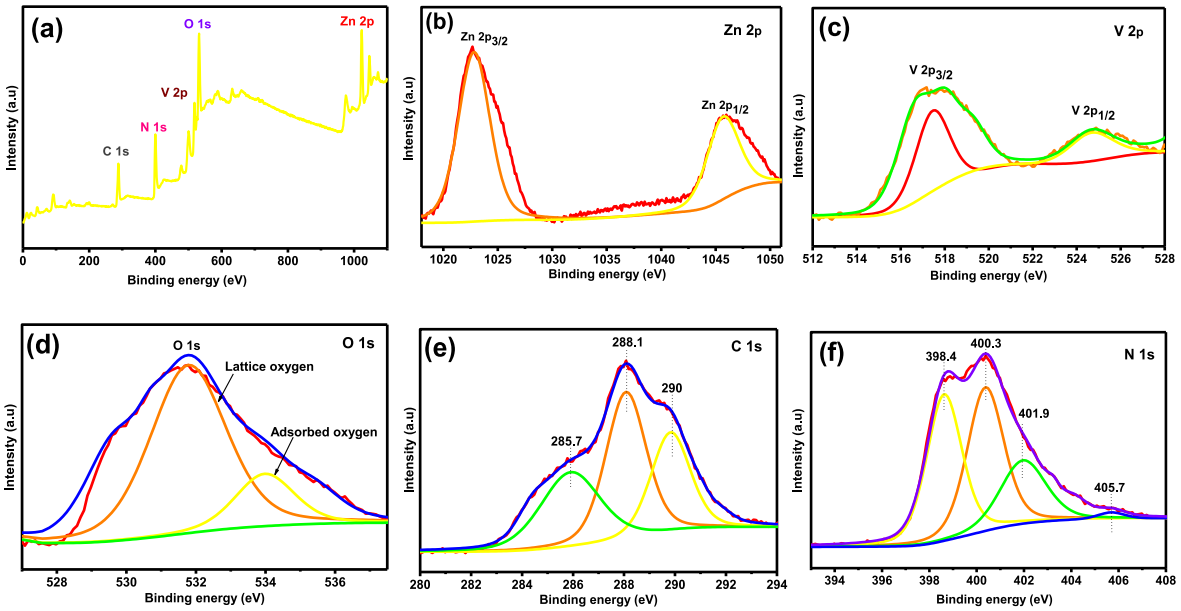

Fig. 4. XPS spectra of ZnV_2O_6/f-C_3N_4 (1:1) : (a) Survey spectrum; (b) Zn 2p; (c) V 2p, (d) O 1s, (e) C 1s, and (f) N 1s.

heterojunction. The SAED pattern of the f-C_3N_4 modified zinc vanadium oxide in Fig. 3(f) exhibits a perspicuous crystalline ring because of considerable crystallization of zinc vanadium oxide.

X-ray photoelectron spectroscopy (XPS) analysis was conducted in order to investigate the elemental composition of the ZnV_2O_6/f-C_3N_4 nanocomposite and the results are presented in Fig. 4. As displayed in Fig. 4(a), XPS survey spectra of ZnV_2O_6/f-C_3N_4 show Zn, V, O, C and N elements. Fig. 4(b) shows two clear signals at 1044.6 and 1021.5 eV, corresponding to Zn $2p_{1/2}$ and Zn $2p_{3/2}$, respectively, which is typical characteristics of Zn^{2+} (Bai et al., 2014). The high-resolution V 2p XPS spectra (Fig. 4(c)) shows two peaks at 524.3 and 517 eV corresponding to V $2p_{1/2}$ and V $2p_{3/2}$, respectively, confirming the presence of V^{5+} (Xiao et al., 2018). Fig. 4(d) exhibits three peaks positioned at 534, 531.7 and 529.6 eV. Peak located at 534 eV can be assigned to the surface-absorbed oxygen species, whereas the peaks at 531.7 and 529.6 eV

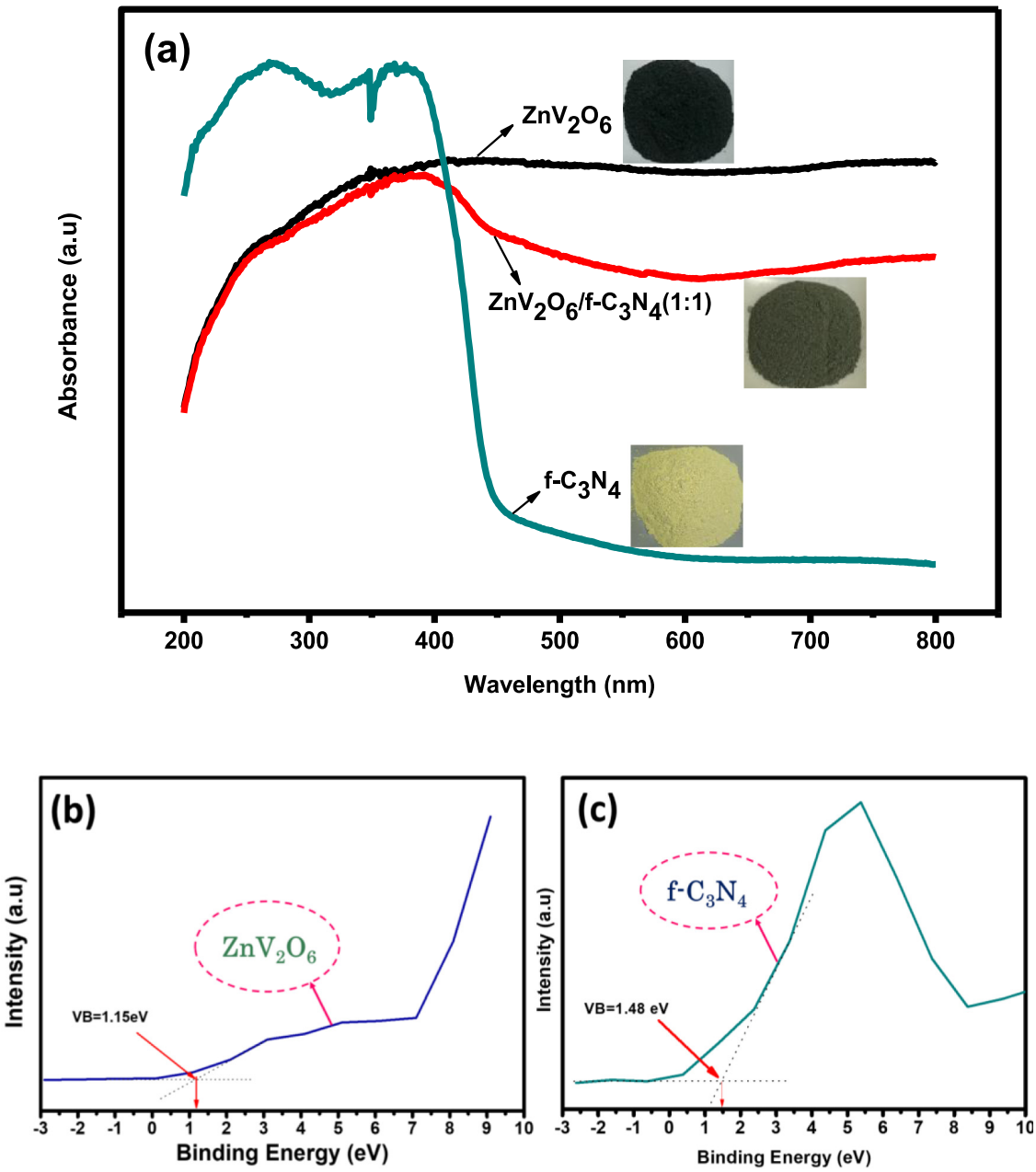

Fig. 5. (a) UV–vis diffuse reflectance absorbance spectra of f-C_3N_4, ZnV_2O_6 and ZnV_2O_6/f-C_3N_4 nanocomposite; (b); Valence band (VB) XPS spectra of ZnV_2O_6; (c) Valence band (VB) XPS spectra of f-C_3N_4.

is attributed to the lattice oxygen species in ZnV_2O_6 photocatalyst (Yin et al., 2017). These findings confirmed the surface element composition of the ZnV_2O_6 photocatalyst. Fig. 4(e) depicts the XPS of C 1s for ZnV_2O_6/f-C_3N_4 nanocomposite. Two clear signals at 284.7 and 288.1 eV belong to sp^2-hybridized carbons and the sp^2-bonded C in N-containing aromatic rings (N–C=N), respectively (Ong et al., 2015). The high-resolution N 1s spectra displayed four peaks at 398.7 eV (sp^2-bonded N atoms, C–N=C), 400.6 eV (ternary N groups, N- $(C)_3$) and 401.8 eV (side N-H groups) as exhibited in Fig. 4(f) (Lu et al., 2014). The small peak at 405.7 eV was owing to the successful functionalization of g- C3N4 (positive charge) (Ong et al., 2015). The acid pre-treatment with HNO_3 can simply alter the gC_3N_4 to possess positive charge that can serve as a mediator and trap for photoexcited electrons.

The optical properties of the f-C_3N_4, ZnV_2O_6 and ZnV_2O_6/f-C_3N_4 samples were measured by DR UV–Vis spectroscopy, and the results are exhibited in Fig. 5(a). The band-gap energies of f-C_3N_4, ZnV_2O_6 and ZnV_2O_6/f-C_3N_4 samples were

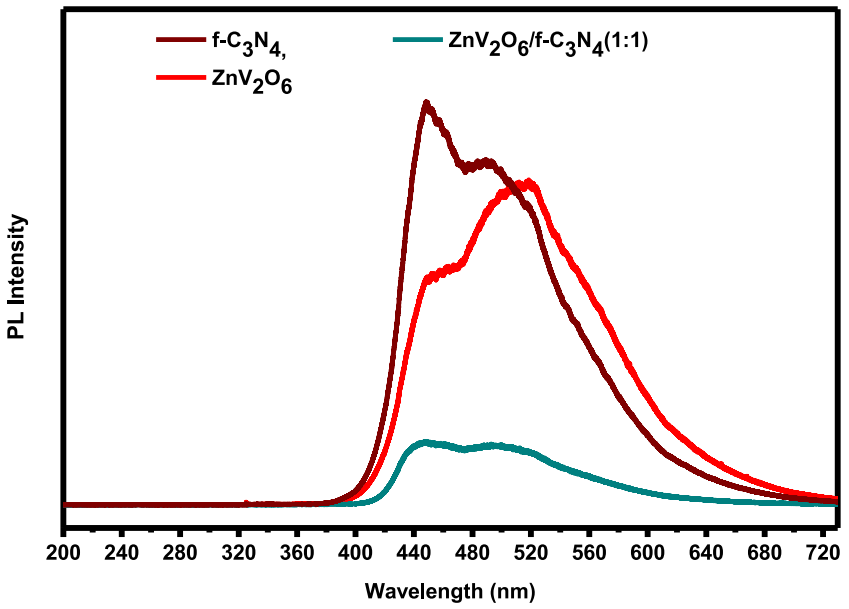

Fig. 6. Photoluminescence (PL) spectra for f-C_3N_4, ZnV_2O_6 and ZnV_2O_6/g-C_3N_4 nanocomposite.

estimated through the Tauc plot of the Kubelka–Munk function. Band-gap energies of 2.6, 2.02 and 2.21 eV were found for the f-C_3N_4, ZnV_2O_6 and ZnV_2O_6/f-C_3N_4 samples, respectively. Based on calculations using the Kubelka–Munk rule, f-C_3N_4 and ZnV_2O_6 combination results in a band gap reduction from 2.6 eV to 2.21 eV. As a result, when compared to pure f-C_3N_4, ZnV_2O_6/f-C_3N_4 shifts toward the visible-light region and reduces the band gap. The band gaps (E_{bg}) of f-C_3N_4 and ZnV_2O_6 photocatalysts were calculated using Tauc equation as displayed in Eq. (1).

$$E_g(eV) = \frac{1240}{\lambda} \tag{1}$$

The wavelengths of the f-C_3N_4 and ZnV_2O_6 samples are 477 and 613 nm at which values of E_g for f-C_3N_4 and ZnV_2O_6 were calculated to be 2.6 and 2.02 eV, respectively. The band position of the conduction bands (E_{CB}) of f-C_3N_4 and ZnV_2O_6 samples were calculated using Eq. (2).

$$E_{VB} = E_{CB} + E_{bg} \tag{2}$$

The valence band energies (E_{VB}) of f-C_3N_4 and ZnV_2O_6 photocatalysts were measured by X-ray photoelectron spectroscopy (XPS). Fig. 5(b) and (c) display the valence band energies of f-C_3N_4 and ZnV_2O_6 photocatalysts located at ∼1.48 and ∼1.15 eV, respectively. The values of E_{bg} for f-C_3N_4 and ZnV_2O_6 photocatalysts are 2.6 and 2.02 eV, respectively. Therefore, the conduction bands of f-C_3N_4 and ZnV_2O_6 photocatalysts were calculated to be −1.12 and −0.87 eV, respectively. Thus, it could be concluded that the valence band of ZnV_2O_6 is higher than f-C_3N_4, and the conduction band of f-C_3N_4 is higher than ZnV_2O_6. This band structure combination would be suitable for enhanced CO_2 conversion to CH_3OH under visible light.

Using the photoluminescence (PL) technique, the charge carrier separation efficiency of semiconductor photocatalysts were further investigated. Fig. 6 displays the PL spectra of f-C_3N_4, ZnV_2O_6, and ZnV_2O_6/f-C_3N_4 samples. The PL spectra of photocatalysts exhibits a strong PL emission band at 500 nm, which can be ascribed to the band to band recombination. It can be seen that the f-C_3N_4 sample has the highest emission intensity in PL spectra. In comparison to g-C_3N_4, the ZnV_2O_6 sample exhibits lower PL intensity. The greater charge carrier separation is produced by the ZnV_2O_6/f-C_3N_4 nanocomposite, which exhibits the lowest emission intensity in PL spectra.

3.2. Photocatalytic activity of photocatalysts

A number of tests were carried out to confirm the generation of CH_3OH during the CO_2 conversion process at atmospheric pressure, room temperature, and feed flow rate of 20 ml/min. The photocatalytic CO_2 process was carried out in the dark during the experiment, and the reaction system did not yield any carbon-containing compounds. This implies that illumination by light is necessary for the CO_2 photocatalytic conversion process. Another experiment was performed utilizing light illuminations, products of CO_2 conversion were not produced without utilizing a photocatalyst. Finally, experiments were performed in the existence of photocatalyst, light illuminations and water, and generation of

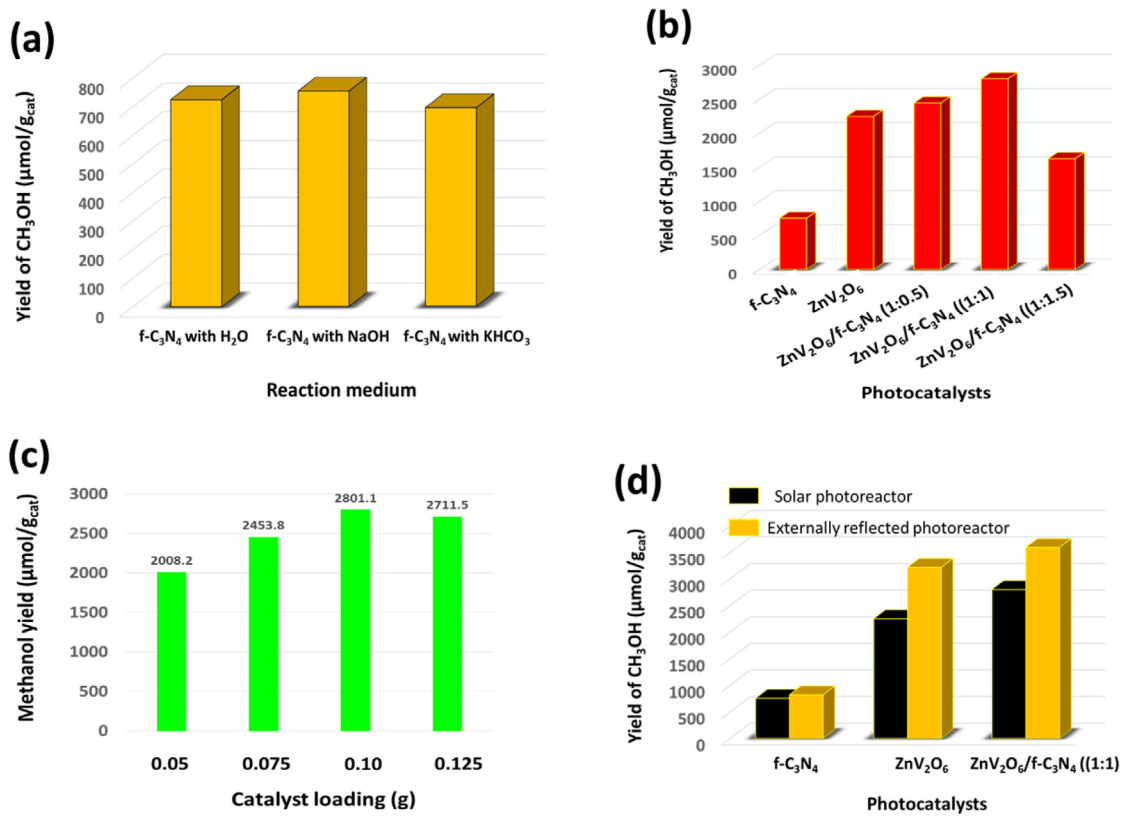

Fig. 7. (a) Yield of methanol for different reaction mediums; (b) Effects of f-C_3N_4 loading on ZnV_2O_6 photoactivity for photocatalytic CO_2 conversion to CH_3OH; (c) The effect of catalyst loading over ZnV_2O_6/f-C_3N_4 nanocomposite; (d) Comparison between solar photoreactor and externally reflected photoreactor for photocatalytic CO_2 conversion over various photocatalysts. Reaction parameters: room temperature, atmospheric pressure, feed flow rate 20 mL/min and irradiation time 2 h.

CH_3OH was obtained. As a result, all the information supports that photocatalytic carbon dioxide is photoactivated in the presence of light illuminations.

The effects of reaction medium are displayed in Fig. 7(a). The efficiency of f-C_3N_4 was tested utilizing water (H_2O), sodium hydroxide (NaOH) solution and potassium bicarbonate ($KHCO_3$) solution. It is clear that CO_2 conversion in the presence of 0.1 M sodium hydroxide registered high CH_3OH yield which is 753.7 µ-mol. g-cat^{-1} for f-C_3N4, 1.041 and 1.086 times higher than utilizing water and potassium bicarbonate, respectively. The drop in potassium bicarbonate yield may be caused by group 1 elements' lattice enthalpies declining as their atomic numbers decrease. Based on their ionization energies, Na ought to be a much better salt than K because it releases electrons simply. Since photoreduction of CO_2 is a multi-step reaction requiring several electrons, Na would be a preferable replacement for K salts. For sodium hydroxide, the flow of exit gas was slower because the reaction between CO_2 and sodium hydroxide obtained HCO_3^- ions. The HCO_3^- was utilized to produce methanol after being exposed to photogenerated electrons on the surface of the photocatalyst. Additionally, highly concentrated OH^- ions in the aqueous solution function as strong hole scavengers and produce OH radicals. As a result, there is an increase in the use of surface electrons, which encourages the conversion of CO_2 to methanol. In the case of water, the outflow of product gas from the system was more rapid compared to that of sodium hydroxide. The CO_2 when dissolved in water only protonates to give CO_3^{2-} ions. Therefore, sodium hydroxide is able to dissolve and convert more CO_2 compared to the other reaction media.

Fig. 7(b) displays the effect of f-C_3N_4 on the efficiency of ZnV_2O_6 for photoreduction of CO_2 to CH_3OH under visible light. Compared to f-C_3N_4, ZnV_2O_6 exhibits higher CH3OH production rates. This clear enhancement can be attributed to the higher surface area and better photo-absorption performance of ZnV_2O_6 compared with f-C_3N_4. Moreover, modified f-C_3N_4 with ZnV_2O_6 has significantly enhanced photoreduction of CO_2 and the nanocomposite ratios 1:1 gives the optimal yield of CH_3OH. The highest generation of CH_3OH with yield 2801 µmol. g-cat^{-1} was produced over ZnV_2O_6/f-C_3N_4 nanocomposite, which were 1.3 and 3.7 times higher than when utilizing ZnV_2O_6 and f-C_3N_4 samples, respectively. This significant enhancement can be assigned to better charge carrier separation across the heterojunction of the ZnV_2O_6/f-C_3N_4 nanocomposite.

The effect of ZnV_2O_6/f-C_3N_4 nanocomposite catalyst loading for CH_3OH production is displayed in Fig. 7(c). It is obvious that increasing the catalyst loading in the water solution increased the formation of CH_3OH. This was evidently caused by

a bigger active site being available for the reaction at a higher catalyst loading. This could also be due to the efficient electron/hole pair separation with electron transfer rate to the catalyst's conduction band. The highest CH_3OH yield (2801.1 μmole g-cat^{-1}) was obtained when the catalyst amount was 0.1 g, owing to a good balance between particle distribution and light across the slurry. However, further increase in catalyst amount led to a reduced CH_3OH yield when compared to the 0.1 g. This lower performance might be the result of the particles' ability to act as a shield, preventing a consistent distribution of light throughout the slurry.

The performance of a solar photoreactor and an externally reflected photoreactor for photocatalytic CO_2 reduction is compared in Fig. 7(d). The f-C_3N_4 and ZnV_2O_6 nanosheets dispersed inside the solar photoreactor exhibit lower photoactivity compared to f-C_3N_4 and ZnV_2O_6 nanosheets dispersed inside the externally reflected photoreactor. The yield of CH_3OH was increased from 753.5 and 2250.5 to 820.9 and 3218.3 μmole g-cat^{-1} by replacing solar photoreactor with externally reflected photoreactor over f-C_3N_4 and ZnV_2O_6 nanosheets, respectively. The production of CH_3OH further increased using externally reflected photoreactor and ZnV_2O_6/f-C_3N_4 nanocomposite. The yield of CH_3OH in externally reflected photoreactor was 3591.2 μmole g-cat $^{-1}$ 1.3 times higher than solar photoreactor over ZnV_2O_6/f-C_3N_4 nanocomposite. This phenomenon can be described based on the intensity of light available for conversion of CO_2. In comparison to an externally reflected photoreactor, the solar photoreactor's light intensity is significantly lower. A reflector was employed in the design of solar photoreactors to reflect light, resulting in stronger light irradiations that increased CO_2 reduction and yield rates. However, the solar photoreactor's reduced yield rate was caused by insufficient light intensity.

Fig. 8(a) compares photocatalytic CO_2 reduction with effect of time over ZnV_2O_6/f-C_3N_4 nanocomposite using solar photoreactor and externally reflected photoreactor. Obviously, the generation of CH_3OH was significant using externally reflected photoreactor compared to solar photoreactor under the same operating conditions. Utilizing externally reflected photoreactor, the CH_3OH yield rate over ZnV_2O_6/f-C_3N_4 nanocomposite was 4665.6 μmole g-cat^{-1} after 10 h of irradiation time, which was 1.25-times higher compared to utilizing solar photoreactor. This was due to higher light distribution and harvesting over the catalyst surface utilizing reflector. In general, the photoactivity of ZnV_2O_6/f-C_3N_4 nanocomposite was improved by the existence of a reflector.

The stability of ZnV_2O_6/f-C_3N_4 nanocomposite was further examined to evaluate the life of catalyst using externally reflected photoreactor under visible light illuminations. All tests were repeated in cyclic runs under the same conditions to examine the stability of ZnV_2O_6/f-C_3N_4 nanocomposite. Fig. 8(b) displays the stability test for photocatalytic CO_2 conversion to CH_3OH for reduction photocatalyst. The photocatalyst was filtered, dried, and reused with fresh reductant following each cycle. The ZnV_2O_6/f-C_3N_4 nanocomposite does not deactivate throughout the three cyclic runs for CH_3OH product, implying it is a very stable nanocomposite under visible light irradiations. However, it was found that the ZnV_2O_6/f-C_3N_4 nanocomposite was extremely stable for the continuous generation of CH_3OH in cyclic runs.

3.3. Mechanism of CO_2 conversion with H_2O

The ZnV_2O_6/f-C_3N_4S-scheme heterojunction are utilized as photocatalysts to evaluate the photocatalytic activity for photocatalytic CO_2 conversion into CH_3OH. The reaction steps during the photocatalytic CO_2 conversion are described briefly in Eqs. (3)–(8).

$$ZnV_2O_6 + hv \rightarrow h^+ + e^- \quad (3)$$

$$g\text{-}C_3N_4 + hv \rightarrow h^+ + e^- \quad (4)$$

$$f\text{-}C_3N_4 + e^- \rightarrow f\text{-}C_3N_4 \quad (5)$$

$$H_2O + h^+ \rightarrow {}^{\bullet}OH + H^+ \quad (6)$$

$$CO_2 + e^- \rightarrow CO_2^{\bullet -} \quad (7)$$

$$CO_2 + 6H^+ + 6e^- \rightarrow CH_3OH + H_2O \quad (8)$$

The generations of photoexcited electron and hole pairs and their trapping via f-C_3N_4 are listed in Eqs. (3) and (5). The reduction of CO_2 occurs at the conduction band (CB) by the activity of electrons and H_2O is oxidized by holes at the valence band (VB) and this is described in Eqs. (6) and (7). The production of CH_3OH through the photo-conversion of CO_2 is displayed in Eq. (8). The reaction scheme for the production of CH_3OH using ZnV_2O_6/f-C_3N_4 S-scheme heterojunction in externally reflected photoreactor is detailed further in Fig. 9(a) and (b).

The energy band theory could be used to further illustrate the photocatalytic CO_2 conversion to CH_3OH over ZnV_2O_6/f-C_3N_4 nanocomposite. Overall, photoexcited electrons could consume efficiently, if the reduction potential of reaction is lower than the CB potential of the semiconductor (Zhang et al., 2022b). In terms of conventional hydrogen electrode vs a thermodynamic reduction potentials at pH 7, the reactions that may occur during the photocatalytic CO_2 conversion with H_2O to generate CH_3OH can be explained by reactions (9)–(12) (Zhao et al., 2012; Zhou et al., 2011).

$$CO_2 + 2H^+ + 2e^- \rightarrow CO + H_2O \quad E^0 = -0.48\ V \quad (9)$$

$$2H^+ + 2e^- \rightarrow H_2 \quad E^0 = -0.41\ V \quad (10)$$

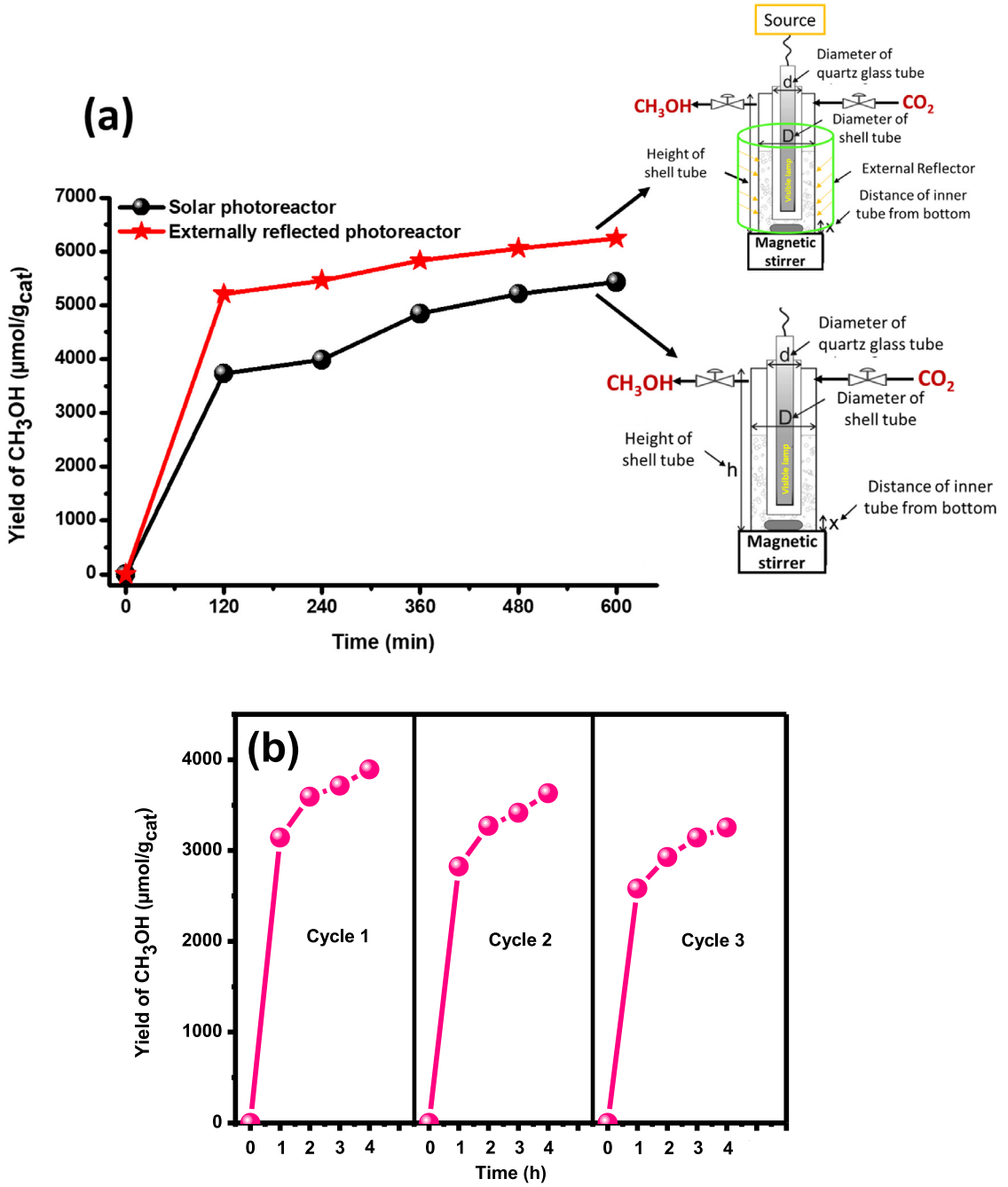

Fig. 8. (a) Comparison of photocatalytic CO_2 conversion with effect of time over ZnV_2O_6/f-C_3N_4 nanocomposite using solar photoreactor and externally reflected photoreactor; (b) Stability study of the ZnV_2O_6/f-C_3N_4 nanocomposite using externally reflected photoreactor.

$$CO_2 + 6H^+ + 6e^- \rightarrow CH_3OH + H_2O \quad E^0 = -0.38\ V \tag{11}$$

$$2H_2O + 4h^+ \rightarrow 4H^+ + O_2 \quad E^0 = +0.82\ V \tag{12}$$

The conduction band of f-C_3N_4 and ZnV_2O_6 nanosheets are $E_{CB} = -1.12$ V and $E_{CB} = -0.87$ V, respectively, at pH 7 which is more likely to drive CO_2 conversion to CH_3OH due to the lower reduction potential difference ($E^o(CO_2/CH_3OH) = -0.38$ V). The reduction potential requires 6 electrons to generate CH_3OH as shown in Eq. (11). Nevertheless, the high rate of CH_3OH yield over ZnV_2O_6/f-C_3N_4 nanosheets in externally reflected photoreactor led to a raised likelihood of multi-electron reactions because of large number of photons reflected by external reflector over the semiconductor surface.

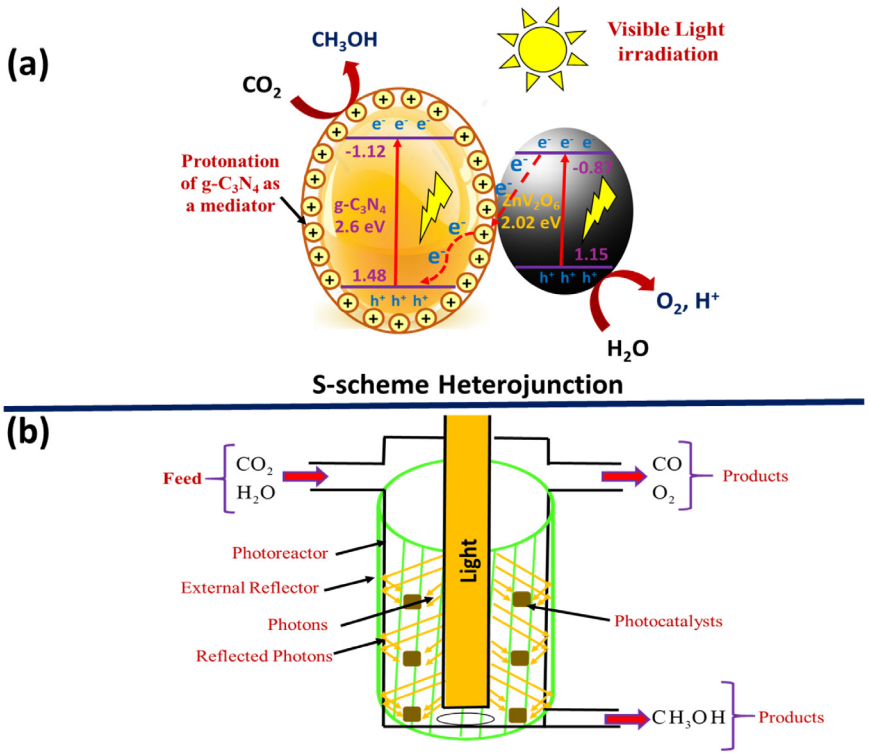

Fig. 9. (a) Schematic of reaction scheme for CO_2 conversion with H_2O to CH_3OH and (b) Reflected photons mechanism through external reflector of solar photoreactor.

4. Conclusions

This study involved the photocatalytic CO_2 conversion with H_2O over ZnV_2O_6/f-C_3N_4 S-scheme photocatalyst in an externally reflected photoreactor. The experimental findings reveal substantial new findings to enhance the effectiveness of CO_2 conversion. The experimental findings demonstrated effective CO_2 photoconversion with H_2O to CH_3OH over ZnV_2O_6/f-C_3N_4 nanocomposite and externally reflected photoreactor compared to pure ZnV_2O_6 and solar photoreactor. The maximum yield rate of CH_3OH was 4665.6 μmole g-cat^{-1}. The amount of CH_3OH produced utilizing externally reflected photoreactor was 1.25-fold more than the amount produced utilizing solar photoreactor. The considerable rise in the yield rate indicated photon energy was efficiently utilized in externally reflected photoreactor compared with solar photoreactor. Thus, it can be concluded that an externally reflected photoreactor is an effective photoreactor for CO_2 photoreduction applications while ZnV_2O_6 is an efficient photocatalyst for increasing yield rates. Additionally, the optimal ZnV_2O_6/f-C_3N_4 nanocomposite displayed high photostability after three successive experimental runs and observed continuous photocatalytic conversion of CO_2 with H_2O to CH_3OH.

CRediT authorship contribution statement

Abdullah Bafaqeer: Methodology, Writing – original draft, Reactions performance and material characterizations. **Muhammad Tahir:** Supervision, Conceptualization, Data curation, Formal analysis, Writing – review & editing. **Nor Aishah Saidina Amin:** Supervision, Writing – review & editing. **Nader Al-Bastaki:** Financial support, Review & editing. **Wahid Ali Hamood Altowayti:** Review & editing. **Hammam Abdurabu Thabit:** Review & editing.

Declaration of competing interest

The authors declare that they have no known competing financial interests or personal relationships that could have appeared to influence the work reported in this paper.

Data availability

No data was used for the research described in the article.

Acknowledgments

The authors would like to extend their gratitude to the Ministry of Education (MOE), Malaysia for the financial support vot number 5F384 and UTM Fundamental Research Grant vot number 21H28. The authors would also like to thank the research council at Kingdom University, Kingdom of Bahrain for its partial financial support of this project.

References

Arumugam, M., Tahir, M., Praserthdam, P., 2022. Effect of nonmetals (b, o, p, and s) doped with porous g-C_3N_4 for improved electron transfer towards photocatalytic CO_2 reduction with water into CH_4. Chemosphere 286, 131765.

Aslam, B., Hu, J., Hafeez, M., Ma, D., AlGarni, T.S., Saeed, M., Abdullah, M.A., Hussain, S., 2021. Applying environmental Kuznets curve framework to assess the nexus of industry, globalization, and CO_2 emission. Environ. Technol. Innov. 21, 101377.

Bafaqeer, A., Tahir, M., Amin, N.A.S., 2018a. Synergistic effects of 2D/2D ZnV_2O_6/RGO nanosheets heterojunction for stable and high performance photo-induced CO_2 reduction to solar fuels. Chem. Eng. J. 334, 2142–2153.

Bafaqeer, A., Tahir, M., Amin, N.A.S., 2018b. Synthesis of hierarchical ZnV_2O_6 nanosheets with enhanced activity and stability for visible light driven CO_2 reduction to solar fuels. Appl. Surf. Sci. 435, 953–962.

Bafaqeer, A., Tahir, M., Amin, N.A.S., Mohamed, A.R., Yunus, M.A.C., 2021. Fabricating 2D/2D/2D heterojunction of graphene oxide mediated g-C_3N_4 and ZnV_2O_6 composite with kinetic modelling for photocatalytic CO_2 reduction to fuels under UV and visible light. J. Mater. Sci. 56 (16), 9985–10007.

Bai, J., Li, X., Liu, G., Qian, Y., Xiong, S., 2014. Unusual formation of $ZnCo_2O_4$ 3D hierarchical twin microspheres as a high-rate and ultralong-life lithium-ion battery anode material. Adv. Funct. Mater. 24 (20), 3012–3020.

Baniamer, M., Aroujalian, A., Sharifnia, S., 2021. Photocatalytic membrane reactor for simultaneous separation and photoreduction of CO_2 to methanol. Int. J. Energy Res. 45 (2), 2353–2366.

Cao, H., Yan, Y., Wang, Y., Chen, F.-F., Yu, Y., 2023. Dual role of g-C_3N_4 microtubes in enhancing photocatalytic CO_2 reduction of Co_3O_4 nanoparticles. Carbon 201, 415–424.

Foulady-Dehaghi, R., Behpour, M., 2020. Visible and solar photodegradation of textile wastewater by multiple doped TiO_2/Zn nanostructured thin films in fixed bed photoreactor mode. Inorg. Chem. Commun. 117, 107–946.

Hussain, N., Abdelkareem, M.A., Alawadhi, H., Elsaid, K., Olabi, A., 2022. Synthesis of Cu-g-C_3N_4/MoS_2 composite as a catalyst for electrochemical CO_2 reduction to alcohols. Chem. Eng. Sci. 258, 117757.

Idris, A.M., Jiang, X., Tan, J., Cai, Z., Lou, X., Wang, J., Li, Z., 2022. Dye-sensitized fe-MOF nanosheets as visible-light driven photocatalyst for high efficient photocatalytic CO_2 reduction. J. Colloid Interface Sci. 607, 1180–1188.

Jebaseelan, S.S., Selvan, N.M., Kumar, C., Kalaimurugan, A., Srujana, A., Ravi, C., 2021. Solving constrained economic electrical energy generation and CO_2 emission dispatch using hybrid algorithm. Environ. Technol. Innov. 24, 101–999.

Ješić, D., Jurković, D.L., Pohar, A., Suhadolnik, L., Likozar, B., 2021. Engineering photocatalytic and photoelectrocatalytic CO_2 reduction reactions: Mechanisms, intrinsic kinetics, mass transfer resistances, reactors and multi-scale modelling simulations. Chem. Eng. J. 407, 126–799.

Khan, A.A., Tahir, M., 2019. Recent advancements in engineering approach towards design of photo-reactors for selective photocatalytic CO_2 reduction to renewable fuels. J. CO_2 Util. 29, 205–239.

Kumar, A., Khosla, A., Sharma, S.K., Dhiman, P., Sharma, G., Gnanasekaran, L., Naushad, M., Stadler, F.J., 2023. A review on S-scheme and dual S-scheme heterojunctions for photocatalytic hydrogen evolution, water detoxification and CO_2 reduction. Fuel 333, 126267.

Kumar, A., Raizada, P., Thakur, V.K., Saini, V., Khan, A.A.P., Singh, N., Singh, P., 2021. An overview on polymeric carbon nitride assisted photocatalytic CO_2 reduction: strategically manoeuvring solar to fuel conversion efficiency. Chem. Eng. Sci. 230, 116–219.

Lee, D.-E., Reddy, K.P., Moru, S., Jo, W.-K., Tonda, S., 2023. Facet-induced charge transfer and photocatalytic performance of an S-scheme hybrid heterojunction composed of porous g-C_3N_4 nanosheets and WO_3 nanorods with exposed high-energy (001) facets. Appl. Surf. Sci. 610, 155569.

Li, L., Ma, D., Xu, Q., Huang, S., 2022a. Constructing hierarchical $ZnIn_2S_4$/g-C_3N_4 S-scheme heterojunction for boosted CO_2 photoreduction performance. Chem. Eng. J. 437, 135153.

Li, H., Wang, D., Miao, C., Wang, Y., Wang, Y., Liu, C., Che, G., 2022b. g-C_3N_4/BiOI s-scheme heterojunction: A 2D/2D model platform for visible-light-driven photocatalytic CO_2 reduction and pollutant degradation. J. Environ. Chem. Eng. 10 (4), 108201.

Liang, S., Altaf, N., Huang, L., Gao, Y., Wang, Q., 2020. Electrolytic cell design for electrochemical CO_2 reduction. J. CO_2 Util. 35, 90–105.

Lu, Z., Wang, Z., 2023. S-scheme $CuWO_4$@g-C_3N_4 core–shell microsphere for CO_2 photoreduction. Mater. Sci. Semicond. Process. 153, 107177.

Lu, X., Xu, K., Chen, P., Jia, K., Liu, S., Wu, C., 2014. Facile one step method realizing scalable production of g-C_3N_4 nanosheets and study of their photocatalytic H_2 evolution activity. J. Mater. Chem. A 2 (44), 18924–18928.

Ng, B.J., Kong, X.Y., Chew, Y.H., Teh, Y.W., Chai, S.P., 2021. Reactors, fundamentals, and engineering aspects for photocatalytic and photoelectrochemical systems. In: Solar-to-Chemical Conversion: Photocatalytic and Photoelectrochemcial Processes. pp. 419–447.

Nguyen, L.T., Vo, D.-V.N., Nguyen, L.T., Duong, A.T., Nguyen, H.Q., Chu, N.M., Nguyen, D.T.C., Van Tran, T., 2022. Synthesis, characterization, and application of $ZnFe_2O_4$@ZnO nanoparticles for photocatalytic degradation of rhodamine b under visible-light illumination. Environ. Technol. Innov. 25, 102130.

Ong, W.-J., Tan, L.-L., Chai, S.-P., Yong, S.-T., Mohamed, A.R., 2015. Surface charge modification via protonation of graphitic carbon nitride (g-C_3N_4) for electrostatic self-assembly construction of 2D/2D reduced graphene oxide (rGO)/g-C_3N_4 nanostructures toward enhanced photocatalytic reduction of carbon dioxide to methane. Nano Energy 13, 757–770.

Sayed, M., Zhu, B., Kuang, P., Liu, X., Cheng, B., Ghamdi, A.A.A., Wageh, S., Zhang, L., Yu, J., 2022. EPR investigation on electron transfer of 2D/3D g-C_3N_4/ZnO S-scheme heterojunction for enhanced CO_2 photoreduction. Adv. Sustain. Syst. 6 (1), 2100264.

Sharma, A., Hosseini-Bandegharaei, A., Kumar, N., Kumar, S., Kumari, K., 2022. Insight into ZnO/carbon hybrid materials for photocatalytic reduction of CO_2: An in-depth review. J. CO_2 Util. 65, 102205.

Szamosvölgyi, Á., Rajkumar, T., Sápi, A., Szenti, I., Ábel, M., Gómez-Pérez, J.F., Baán, K., Fogarassy, Z., Dodony, E., Pécz, B., 2022. Interfacial Ni active sites strike solid solutional counterpart in CO_2 hydrogenation. Environ. Technol. Innov. 27, 102747.

Tahir, M., Amin, N.A.S., 2017. Photo-induced CO_2 reduction by hydrogen for selective CO evolution in a dynamic monolith photoreactor loaded with Ag-modified TiO_2 nanocatalyst. Int. J. Hydrog. Energy 42 (23), 15507–15522.

Tahir, M., Tahir, B., 2020. Constructing a stable 2D/2D heterojunction of oxygen-cluster-modified Ti_3AlC_2 MAX cocatalyst with proton-rich C_3N_4 for highly efficient photocatalytic CO_2 methanation. Ind. Eng. Chem. Res. 59 (21), 9841–9857.

Tahir, M., Tahir, B., 2022. Constructing S-scheme 2D/0D g-C_3N_4/TiO_2 NPs/MPs heterojunction with 2D-Ti_3AlC_2 MAX cocatalyst for photocatalytic CO_2 reduction to CO/CH_4 in fixed-bed and monolith photoreactors. J. Mater. Sci. Technol. 106, 195–210.

Thabit, H.A., Kabir, N.A., Ismail, A.K., Alraddadi, S., Bafaqeer, A., Saleh, M.A., 2022. Development of Ag-doped ZnO thin films and thermoluminescence (TLD) characteristics for radiation technology. Nanomaterials 12 (17), 3068.

Wang, K., Feng, X., Shangguan, Y., Wu, X., Chen, H., 2022a. Selective CO_2 photoreduction to CH_4 mediated by dimension-matched 2D/2D Bi_3NbO_7/g-C_3N_4 S-scheme heterojunction. Chin. J. Catal. 43 (2), 246–254.
Wang, H., Li, J., Wan, Y., Nazir, A., Song, X., Huo, P., Wang, H., 2023. Fabrication of Zn vacancies-tunable ultrathin-g-C_3N_4@$ZnIn_2S_4$/SWNTs composites for enhancing photocatalytic CO_2 reduction. Appl. Surf. Sci. 613, 155989.
Wang, H., Li, X., Zhao, X., Li, C., Song, X., Zhang, P., Huo, P., 2022b. A review on heterogeneous photocatalysis for environmental remediation: From semiconductors to modification strategies. Chin. J. Catal. 43 (2), 178–214.
Wang, L., Zhu, B., Zhang, J., Ghasemi, J.B., Mousavi, M., Yu, J., 2022c. S-scheme heterojunction photocatalysts for CO_2 reduction. Matter 5 (12), 4187–4211.
Xiao, B., Huang, H., Yu, X., Song, J., Qu, J., 2018. Facile synthesis of layered V_2O_5/ZnV_2O_6 heterostructures with enhanced sensing performance. Appl. Surf. Sci. 447, 569–575.
Xu, Q., Wageh, S., Al-Ghamdi, A.A., Li, X., 2022. Design principle of S-scheme heterojunction photocatalyst. J. Mater. Sci. Technol. 124, 171–173.
Yazdani, D., Zinatizadeh, A.A., Joshaghani, M., 2018. Organic–inorganic Z-scheme g-C_3N_4-N_iT_i-layered double hydroxide films for photocatalytic applications in a fixed-bed reactor. J. Ind. Eng. Chem. 63, 65–72.
Yin, Z., Qin, J., Wang, W., Cao, M., 2017. Rationally designed hollow precursor-derived $Zn_3V_2O_8$ nanocages as a high-performance anode material for lithium-ion batteries. Nano Energy 31, 367–376.
Yuan, H., Cheng, B., Lei, J., Jiang, L., Han, Z., 2021. Promoting photocatalytic CO_2 reduction with a molecular copper purpurin chromophore. Nat. Commun. 12 (1), 1–9.
Zahedi, R., Ayazi, M., Aslani, A., 2022. Comparison of amine adsorbents and strong hydroxides soluble for direct air CO_2 capture by life cycle assessment method. Environ. Technol. Innov. 28, 102854.
Zhang, Z., Cao, Y., Zhang, F., Li, W., Li, Y., Yu, H., Wang, M., Yu, H., 2022a. Tungsten oxide quantum dots deposited onto ultrathin CdIn2S4 nanosheets for efficient S-scheme photocatalytic CO_2 reduction via cascade charge transfer. Chem. Eng. J. 428, 131–218.
Zhang, T., Shen, Y., Qiu, Y., Liu, Y., Xiong, R., Shi, J., Wei, J., 2017. Facial synthesis and photoreaction mechanism of BiFeO3/Bi2Fe4O9 heterojunction nanofibers. ACS Sustain. Chem. Eng. 5 (6), 4630–4636.
Zhang, L., Zhang, J., Yu, H., Yu, J., 2022b. Emerging S-scheme photocatalyst. Adv. Mater. 34 (11), 2107668.
Zhao, C., Krall, A., Zhao, H., Zhang, Q., Li, Y., 2012. Ultrasonic spray pyrolysis synthesis of Ag/T_iO_2 nanocomposite photocatalysts for simultaneous H_2 production and CO_2 reduction. Int. J. Hydrog. Energy 37 (13), 9967–9976.
Zhao, X., Li, J., Li, X., Huo, P., Shi, W., 2021. Design of metal–organic frameworks (MOFs)-based photocatalyst for solar fuel production and photo-degradation of pollutants. Chin. J. Catal. 42 (6), 872–903.
Zhao, X., Xu, M., Song, X., Zhou, W., Liu, X., Yan, Y., Huo, P., 2022. Charge separation and transfer activated by covalent bond in UiO-66-NH_2/RGO heterostructure for CO_2 photoreduction. Chem. Eng. J. 437, 135210.
Zhou, Y., Tian, Z., Zhao, Z., Liu, Q., Kou, J., Chen, X., Gao, J., Yan, S., Zou, Z., 2011. High-yield synthesis of ultrathin and uniform Bi_2WO_6 square nanoplates benefitting from photocatalytic reduction of CO_2 into renewable hydrocarbon fuel under visible light. ACS Appl. Mater. Interfaces 3 (9), 3594–3601.